





Critical role of device geometry for the phase diagram of twisted bilayer grapheneZachary A. H. Goodwin,¹ Valerio Vitale ,¹ Fabiano Corsetti,¹ Dmitri K. Efetov ,²
Arash A. Mostofi ,¹ and Johannes Lischner ¹¹*Departments of Materials and Physics and the Thomas Young Centre for Theory and Simulation of Materials, Imperial College London, South Kensington Campus, London SW7 2AZ, United Kingdom*²*ICFO - Institut de Ciències Fòniques, The Barcelona Institute of Science and Technology, Castelldefels, Barcelona 08860, Spain*

(Received 20 November 2019; revised manuscript received 4 February 2020; accepted 10 March 2020; published 9 April 2020)

The effective interaction between electrons in two-dimensional materials can be modified by their environment, enabling control of electronic correlations and phases. Here, we study the dependence of electronic correlations in twisted bilayer graphene (tBLG) on the separation to the metallic gate(s) in two device configurations. Using an atomistic tight-binding model, we determine the Hubbard parameters of the flat bands as a function of gate separation, taking into account the screening from the metallic gate(s), the dielectric spacer layers, and the tBLG itself. We determine the critical gate separation at which the Hubbard parameters become smaller than the critical value required for a transition from a correlated insulator state to a (semi)metallic phase. We show how this critical gate separation depends on twist angle, doping, and the device configuration. These calculations may help rationalize the reported differences between recent measurements of tBLG's phase diagram and suggest that correlated insulator states can be screened out in devices with thin dielectric layers.

DOI: [10.1103/PhysRevB.101.165110](https://doi.org/10.1103/PhysRevB.101.165110)**I. INTRODUCTION**

Twisted bilayer graphene (tBLG) has emerged as a highly tunable platform (through twist angle, hydrostatic pressure, and doping) for studying the behavior of correlated electrons in two dimensions [1–8]. Several groups have reported the experimental observation of correlated insulator states in both doped and undoped tBLG near the magic twist angle [1–4]. Despite much theoretical work, no consensus has yet been reached regarding the microscopic mechanism of these phases [9–25]. Superconductivity is also found at low temperatures [2–4], but neither the nature of the pairing interaction nor the symmetry of the superconducting order parameter have been determined.

Importantly, significant differences in the measured phase diagrams have been reported [1–4]: some groups have found correlated insulator states at doping levels where other groups find semimetallic or metallic behavior [1–4]. Similarly, superconductivity is not always found at the same doping levels, and their transition temperatures can be quite different [2–4]. It has been suggested that these differences are a consequence of the varying degree of twist-angle homogeneity in the tBLG samples [4].

Another potential origin of the variations in the observed phase diagram is differences in the device setups employed in the experiments. For example, Cao *et al.* [1,2] used devices in which the tBLG is encapsulated by hexagonal boron-nitride (hBN) slabs of 10–30-nm thickness with gold gates on either side. In contrast, Yankowitz *et al.* [3] used thicker hBN slabs (30–60 nm) sandwiched between two graphite gates, and the device of Lu *et al.* [4] only had a single graphite gate separated from the tBLG by a hBN layer of ~ 10 nm thickness.

The device setup is important because the dielectric environment in which tBLG is situated will have a strong influence

on the screened interaction between the electrons in tBLG [26], which will in turn affect the phase diagram. For gated tBLG devices, the potential induced by an electron in the tBLG is reduced by the image charge in the metallic gate(s). The strength of the resulting effective interaction between electrons in the tBLG is determined by the separation of the metallic gate(s) from the tBLG which can be experimentally controlled via the thickness of a dielectric spacer layer (typically hBN).

In this paper, we investigate the dependence of electron correlations in tBLG devices on the distance between tBLG and the metallic gate(s) (or equivalently, the thickness of the hBN layer). Starting from an atomistic tight-binding model, we construct Wannier functions of the flat bands and calculate the corresponding Hubbard parameters taking into account screening from the metallic gates, the hBN and the tBLG itself. We find that the Hubbard parameters depend sensitively on the gate distance enabling precise control of electron correlations via device geometry. Using results from previous many-body calculations of tBLG [27], we determine the critical gate distances at which the correlated insulator states disappear and predict phase diagrams as function of doping. We also discuss the interplay of device geometry and superconductivity and hypothesize that small gate separations should weaken correlated insulator states, but strengthen superconducting phases.

II. METHODS

To model the electronic structure of tBLG near the magic angle, we employ the techniques described in detail in Refs. [28,29]. For convenience, we summarize briefly the method here. To obtain the electronic band structure of tBLG,

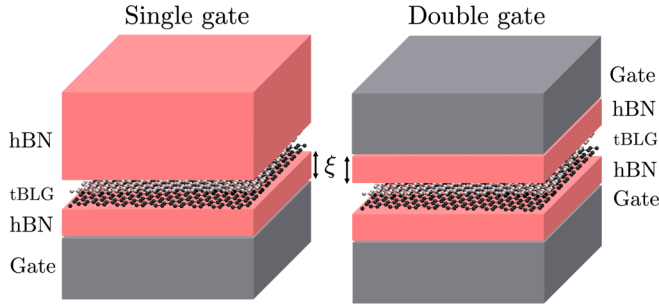


FIG. 1. Twisted bilayer graphene devices with a single gate (left) and two gates (right). The separation between the tBLG and the gate(s) is denoted by ξ . For the double-gated device, the separation is set to be equal on either side.

we carry out atomistic tight-binding calculations using the parameters of Ref. [30]. Next, Wannier functions $w_i(\mathbf{r})$ (with i denoting both the unit cell and the bandlike index of the Wannier function) of the flat bands are generated [28,29,31–34]. The Hubbard parameters of the flat band electrons are obtained by evaluating

$$V_{ij} = \iint d\mathbf{r}d\mathbf{r}' |w_i(\mathbf{r}')|^2 W(\mathbf{r} - \mathbf{r}') |w_j(\mathbf{r})|^2, \quad (1)$$

where $W(\mathbf{r} - \mathbf{r}')$ denotes the screened interaction between electrons, which is determined by screening processes inside tBLG (internal screening), but also has contributions from the environment.

In a typical device configuration, the tBLG is encapsulated by a dielectric substrate [usually hexagonal boron nitride (hBN)] which separates it from the metallic gate(s). Here, we investigate two device types: (i) tBLG with a bottom gate only (i.e., gate/hBN/tBLG/hBN, where it is assumed that the hBN on top is very thick and can be approximated by a semi-infinite dielectric, while the hBN layer that separates the tBLG and the gate has a thickness ξ ; see left panel of Fig. 1), and (ii) tBLG with both a top and a bottom gate (i.e., gate/hBN/tBLG/hBN/gate, where both hBN layers have the same thickness ξ ; see right panel of Fig. 1). The gates are modelled as semi-infinite ideal metals.

For the single-gate device, the electrostatic image charge interaction results in a screened interaction of the form

$$W(\mathbf{r} - \mathbf{r}') = \frac{e^2}{4\pi\epsilon_0\epsilon_r} \left[\frac{1}{|\mathbf{r} - \mathbf{r}'|} - \frac{1}{|2\xi\mathbf{e}_z + \mathbf{r} - \mathbf{r}'|} \right], \quad (2)$$

where e is the electron charge, ϵ_0 is the permittivity of free space, and ϵ_r denotes the dielectric constant due to screening from the tBLG and the hBN. We have assumed that the tBLG lies in the xy plane (\mathbf{e}_z denotes the unit vector pointing in the z direction) and that ξ corresponds to the thickness of hBN (distance from the metallic gate to the bottom of the tBLG). In principle, the internal screening from the tBLG leads to a complicated wave-vector dependent dielectric function, but Goodwin *et al.* [29] previously showed that—near the magic angle—the Hubbard parameters within the constrained random-phase approximation (cRPA) can be accurately reproduced using a bare Coulomb interaction divided by the cRPA dielectric constant of a decoupled bilayer graphene (8.86) [29]. To describe the screening by the dielectric substrate we

add to this the bulk dielectric constant of hBN (3.9) [35] and subtract one to avoid double-counting the dielectric constant of free space resulting in $\epsilon_r = 11.76$.

For the double-gate device, the screened interaction is given by [36]

$$W(\mathbf{r} - \mathbf{r}') = \frac{e^2}{4\pi\epsilon_r\epsilon_0} \sum_{n=-\infty}^{+\infty} \frac{(-1)^n}{\sqrt{|\mathbf{r} - \mathbf{r}'|^2 + (2\xi n)^2}}. \quad (3)$$

For in-plane distances much smaller than ξ , this screened interaction reduces to the bare Coulomb interaction divided by ϵ_r . For in-plane distances much larger than ξ , the screened interaction can be expressed as $W(r) = e^2 e^{-\pi r/\xi} / (2\pi\epsilon_r\epsilon_0\sqrt{r\xi})$ [36]. Here we assume that in the image-potential the tBLG resides in the $z = 0$ plane, which again means ξ corresponds to the thickness of the hBN spacer.

III. RESULTS AND DISCUSSION

Figure 2(a) shows the on-site Hubbard parameter V_{00} of tBLG as a function of the gate separation ξ for a twist angle of 1.12° , for both single-gate and double-gate device configurations (other twist angles are shown in Fig. 4 of Appendix A). The largest values of V_{00} are obtained for large gate separations, and there is a substantial reduction in V_{00} as the gate separation decreases below the moiré length (indicated by the vertical line in Fig. 2). This can be understood from Eqs. (2) and (3) where the image charge contribution arising from the induced charge density at the surface of the gate reduces the Coulomb interaction between electrons in the tBLG. In the case of the single-gate device, when ξ is small, the electron in the tBLG and its image charge effectively interact with other electrons via a weak dipolar potential (instead of the usual monopole charge-charge interaction). For the double-gate setup, the image charges in both gates give rise to an exponentially screened interaction between electrons in the tBLG. The results for V_{00} in the two different device configurations are qualitatively similar, but the Hubbard parameters are somewhat smaller for the double-gate setup since both of the gates contribute to the screening.

In the Hubbard model [37,38], electron-electron interactions are assumed to be short-ranged and the strength of electron correlations is usually measured by the ratio of the on-site Hubbard parameter V_{00} and the nearest-neighbor hopping parameter t . A system with long-ranged electron-electron interactions can be mapped onto an effective Hubbard model with an on-site Hubbard parameter $U^* = V_{00} - V_{01}$ (reflecting the energy required to hop from an empty Wannier orbital to an occupied neighbor site) [39], where V_{01} is the interaction between Wannier functions centered on neighboring AB/BA regions [28,29] (see Fig. 4 of Appendix A for V_{01} as a function of ξ). Figure 2(b) shows U^* for tBLG as function of ξ for a twist angle of 1.12° for both device configurations (results for other twist angles are shown in Fig. 4 of Appendix A). It can be seen that U^* is significantly smaller than V_{00} , indicating that interactions between neighboring Wannier functions play an important role even in the presence of metallic gates [28,29]. This is expected as there is significant overlap between lobes of neighboring Wannier functions [28,31]. Similarly to V_{00} , U^* approaches

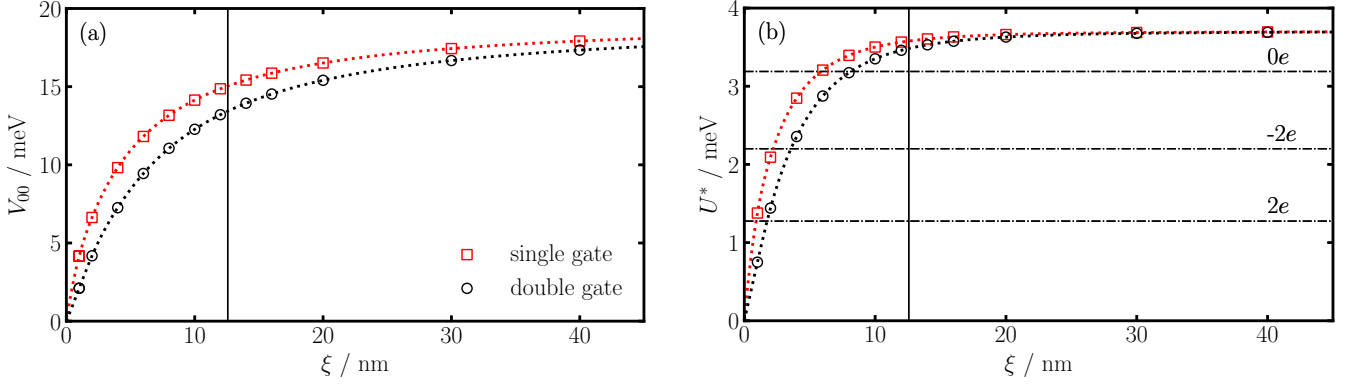


FIG. 2. (a) On-site Hubbard parameter V_{00} as a function of distance ξ between tBLG and the metallic gate(s) for a twist angle of 1.12° for the single-gate and double-gate device (see Fig. 1 for device geometries). (b) Long-range corrected on-site Hubbard parameter U^* as a function of ξ for a twist angle of 1.12° for the single-gate and double-gate device. The horizontal dotted-dashed lines denote critical values of U^* obtained by multiplying the critical U^*/t values from atomistic RPA calculations of tBLG [27] with the hopping parameter for neighboring moiré Wannier functions. Dotted lines through the data points correspond to fits that are used to extract critical gate separations in Fig. 3. The solid vertical line denotes the length of the moiré unit cell.

a constant value in the limit of distant gates, but does so more rapidly once ξ becomes larger than the moiré length. Moreover, U^* exhibits a significantly sharper reduction as the distance decreases. Naively, one might expect that the presence of gates should lead to an *increase* in U^* if the screened interaction is sufficiently short-ranged such that V_{01} is strongly reduced. We find indeed that V_{01} decreases more quickly than V_{00} (see Appendix A), but this *relative* reduction of V_{01} compared to V_{00} is not sufficient to overcome the large *absolute* reduction of V_{00} [see Fig. 2(a)] and, therefore, the overall balance is such that U^* decreases with decreasing ξ .

A. Correlated insulators

When U^*/t reaches a critical value, a phase transition from a (semi)metallic phase to a correlated insulator state is expected. For tBLG, no consensus has yet been reached regarding the nature of the correlated insulator states, nor the corresponding value of the critical U^*/t . For Bernal stacked bilayer graphene, quantum Monte Carlo calculations have found a critical value of 2.2 for a phase transition to a gapped antiferromagnetic phase [40]. Recently, Klebl and Honerkamp calculated the phase diagram of tBLG using an atomistic RPA approach [27]. For undoped tBLG (denoted $0e$), they find a transition from a semimetal to an antiferromagnetic insulator, and for doping levels corresponding to two extra electrons ($-2e$) or holes ($+2e$) per moiré cell, a transition from a metallic phase to a ferromagnetic insulator is predicted. The RPA value for the critical U^*/t in tBLG is smaller than in the Bernal stacked bilayer, and depends both on temperature and doping [27]. Because of the lack of self-energy corrections, the critical U^*/t values from the RPA should be considered as lower bounds [27].

In Fig. 2(b), the critical values of U^* for the cases of $0e$, $-2e$, and $+2e$ doping are indicated by horizontal dotted-dashed lines. Here, we have multiplied the critical U_{p_z}/t_{p_z} values (where U_{p_z} and t_{p_z} denote the Hubbard and hopping parameters of carbon p_z orbitals in tBLG) from Klebl and Honerkamp [27] at a temperature $T \approx 0.3$ K with the hopping

parameter t between neighboring Wannier functions (calculated from the width Δ of the flat bands in our atomistic tight-binding model using $t = \Delta/6$, which is the relation between bandwidth and hopping in graphene). While this procedure is not rigorous, we believe that the resulting critical U^*/t values for the flat-band electrons are useful estimates as there is a close connection between atomistic and low-energy Hamiltonians in tBLG [41]. Moreover, we note that our results for the critical gate distances that are derived from the critical U^*/t values are in good agreement with recent measurements [42,43]. Future work should be carried out to determine the critical U^*/t values of the flat-band electrons in tBLG.

For the single-gate (double-gate) device, as the gate separation is reduced to $\xi_c = 5.86$ nm ($\xi_c = 8.14$ nm), U^* crosses the critical value for zero doping, indicating that tBLG would exhibit a semimetallic phase at zero doping, but the correlated insulator states at $-2e$ and $+2e$ doping would remain. At $\xi_c = 2.21$ nm ($\xi_c = 3.56$ nm), the critical U^* for $-2e$ doping is crossed and finally, at $\xi_c = 0.89$ nm ($\xi_c = 1.74$ nm) the critical value for $+2e$ doping is reached. For even smaller values of ξ , the tBLG is either metallic or semimetallic at the doping levels considered here. These results demonstrate that the phase diagram of tBLG can be controlled via the thickness of the dielectric substrate that separates the tBLG from the metallic gates and, hence, determines the degree to which the gate is able to screen electron-electron interactions in tBLG. The critical separations for phase transitions depend on the device configuration, with smaller values for single-gate devices because the screening is weaker than in double-gate devices.

The critical gate separation ξ_c also depends on the twist angle. Figure 3 shows this dependence as a function of twist angle from the magic angle $\theta^* = 1.18^\circ$ for the single-gate device configuration and for three doping levels: $-2e$ (left panel), $0e$ (middle panel), and $+2e$ (right panel) at $T \approx 0.3$ K. The results for the double-gate configuration are shown in Fig. 7 of Appendix B. For all doping levels, ξ_c decreases as the magic angle is approached. Close to the magic angle, the hopping approaches zero and extremely small values of U^* must be achieved to reach the critical value of U^*/t . This is

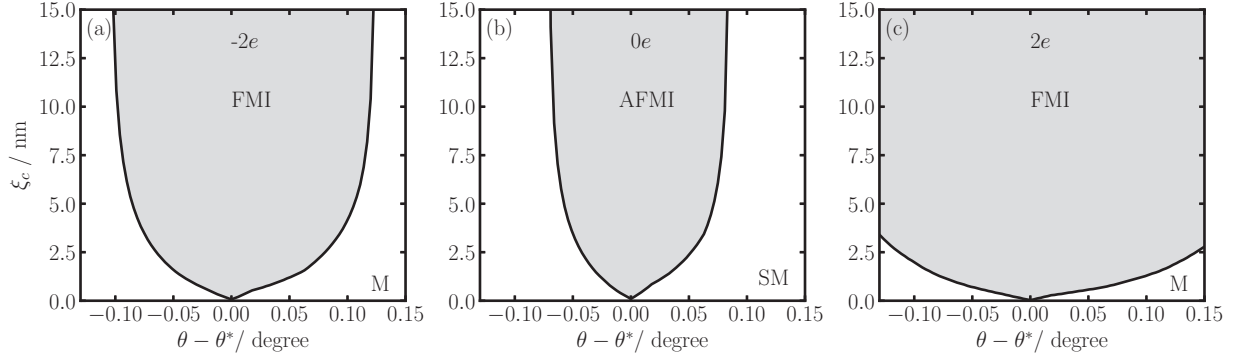


FIG. 3. Critical value of gate distance as a function of twist angle for (a) two additional electrons per moiré unit cell ($-2e$), (b) charge neutrality ($0e$), and (c) two additional holes per moiré unit cell ($2e$) for a device with a single gate. The grey regions indicate correlated insulator states [either ferromagnetic insulators (FMIs) or antiferromagnetic insulators (AFMIs)], while the white regions denotes either metallic (M) or semimetallic (SM) phases. Note that we employ the critical U^*/t values obtained from atomistic RPA calculations of tBLG [27].

only possible for very small values of ξ . Comparing the three doping levels, we find that ξ_c for the undoped system increases most rapidly away from the magic angle. At twist angles larger than 0.1° from the magic angle, the undoped system is always metallic and no phase transition to a correlated insulator phase can be induced. For $-2e$ doping, the critical twist angle window is larger than for zero doping. For $+2e$ doping, a critical thickness can be found for all considered twist angles near the magic angle. At larger temperatures, the critical value of U^*/t is smallest at charge neutrality [27], which means that charge neutrality will require the thinnest hBN slabs to reach the critical value for a phase transition to a (semi)metallic state. In Figs. 8 and 9 of Appendix C we show analogous phase diagrams for both device structures at $T \approx 5$ K.

B. Superconductivity

The thickness ξ of the dielectric spacer layer also influences the stability of the superconducting state which competes with the correlated insulator states discussed above. To bind electrons into Cooper pairs, the effective electron-electron interaction must contain an attractive part V_{att} (this could arise either from electron-phonon coupling, exchange of spin fluctuations, plasmons, or any other glue). The total interaction can be expressed as the sum of the bare Coulomb interaction and V_{att} . The superconducting transition temperature is approximately given by $T_c \propto E_{\text{glue}}/k_B \times \exp[-1/(\lambda - \mu^*)]$, where λ describes the coupling of the electrons to the glue (which has an energy scale E_{glue}) and μ^* is the Coulomb pseudopotential, which describes the repulsion due to the bare Coulomb interaction [44] (k_B is the Boltzmann constant). In the presence of metallic gates, the repulsive bare interaction is reduced by the image charge interaction. As a consequence, μ^* is also reduced and has a dependence on the gate separation ξ . The presence of gates, therefore, should enhance the stability of the superconducting phase and increase the superconducting transition temperature, while reducing the stability of the correlated insulator states. Further calculations are required to quantitatively study the competition between superconductivity and correlated insulator states in the presence of metallic gates.

IV. SUMMARY

We have demonstrated the importance of the device geometry for electron correlations and the phase diagram of twisted bilayer graphene. By reducing the separation between the tBLG and the metallic gate(s), the on-site Hubbard parameter can be reduced to a value smaller than the critical value required for a phase transition from a correlated insulator state to a (semi)metallic state. We have calculated the critical gate-tBLG separation at which correlated insulator states disappear and studied its dependence on twist angle for different doping levels and device configurations. For a fixed twist angle, the phase diagram as function of doping of tBLG depends sensitively on the device geometry which could explain the differences reported by various experimental groups. This opens up the exciting possibility to precisely control electronic phases in tBLG through device engineering.

ACKNOWLEDGMENTS

We thank D. Kennes, C. Karrasch, and A. Khedri for helpful discussions. Z.A.H.G. was supported through a studentship in the Centre for Doctoral Training on Theory and Simulation of Materials at Imperial College London funded by the EPSRC (Grant No. EP/L015579/1). We acknowledge funding from EPSRC Grant No. EP/S025324/1 and the Thomas Young Centre under Grant No. TYC-101.

APPENDIX A: HUBBARD PARAMETERS AT DIFFERENT TWIST ANGLES

Figure 4 shows the variation of the Hubbard parameters as a function of the separation ξ of the gate(s) from the tBLG for a range of twist angles close to the magic angle. The panels on the left-hand (right-hand) side correspond to the single-gate (double-gate) device configuration. For the on-site Hubbard parameter V_{00} [Figs. 4(a) and 4(b)], it is known that they scale linearly with the twist angle at small angles [1,28]. All twist angles, therefore, exhibit a similar dependence on the separation to the gate, but with the magnitude of V_{00} scaled according to the twist angle.

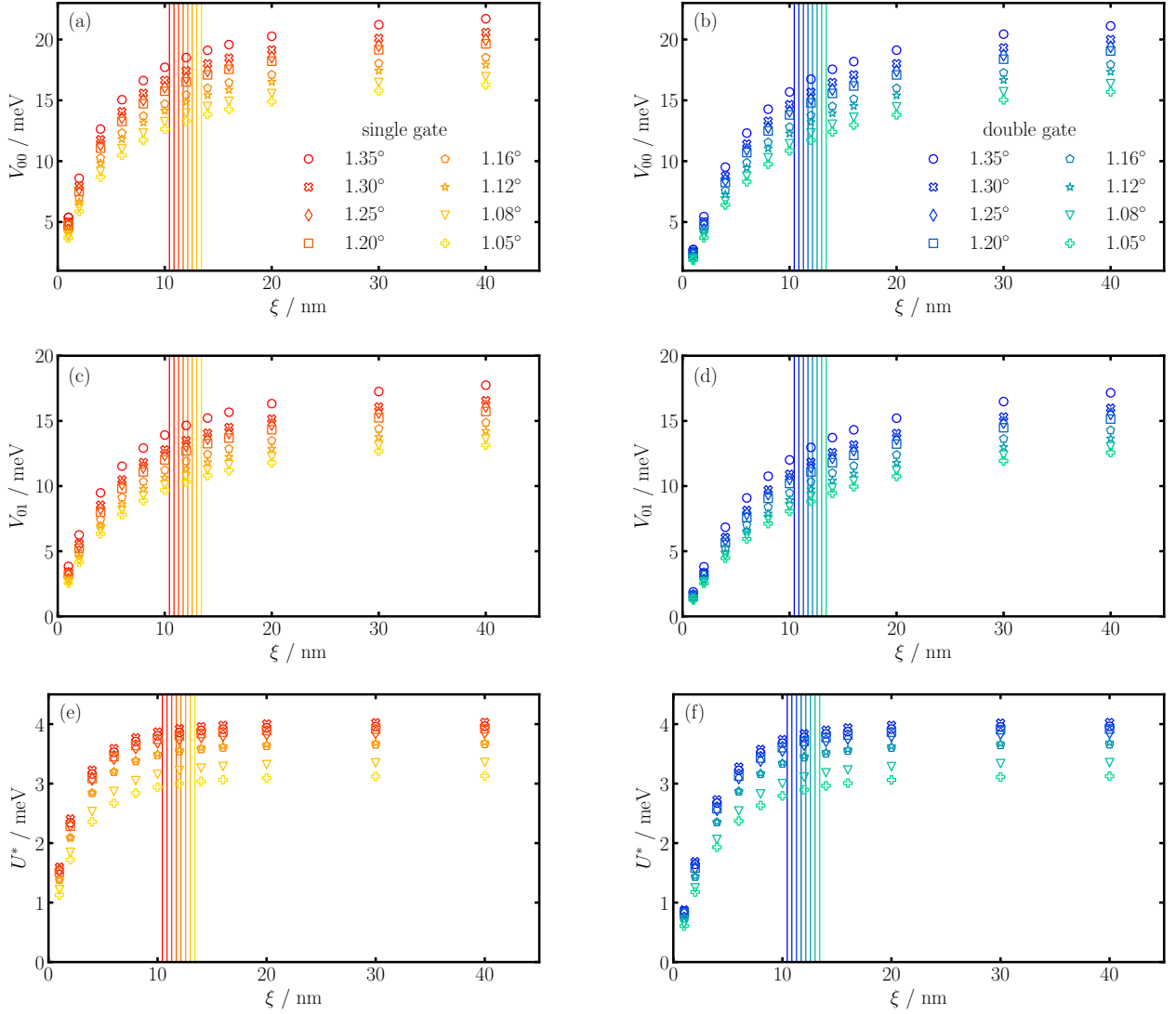


FIG. 4. Hubbard parameters as a function of the separation ξ of the metallic gate(s) from the tBLG for several twist angles (indicated in the legend). The panels in the left-hand (right-hand) column are for the single-gate (double-gate) configuration. (a),(b) On-site Hubbard parameters V_{00} ; (c),(d) nearest-neighbor Hubbard parameters V_{01} ; (e),(f) long-ranged corrected on-site Hubbard parameters U^* . The vertical lines correspond to the moiré unit cell length for each twist angle.

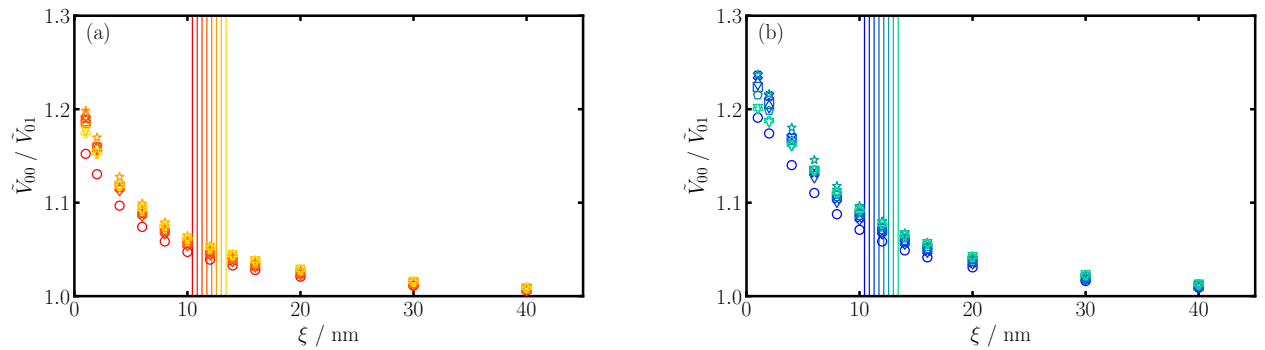


FIG. 5. Ratio of on-site Hubbard parameter [$\tilde{V}_{00} = V_{00}(\xi)/V_{00}(\infty)$] to the nearest-neighbor Hubbard parameter [$\tilde{V}_{01} = V_{01}(\xi)/V_{01}(\infty)$], both of which are rescaled to their Coulomb limit value, as a function of gate separation for the studied twist angles (same color and symbol coding as Fig. 4). (a) Single-gate device configuration; (b) double-gate device configuration.

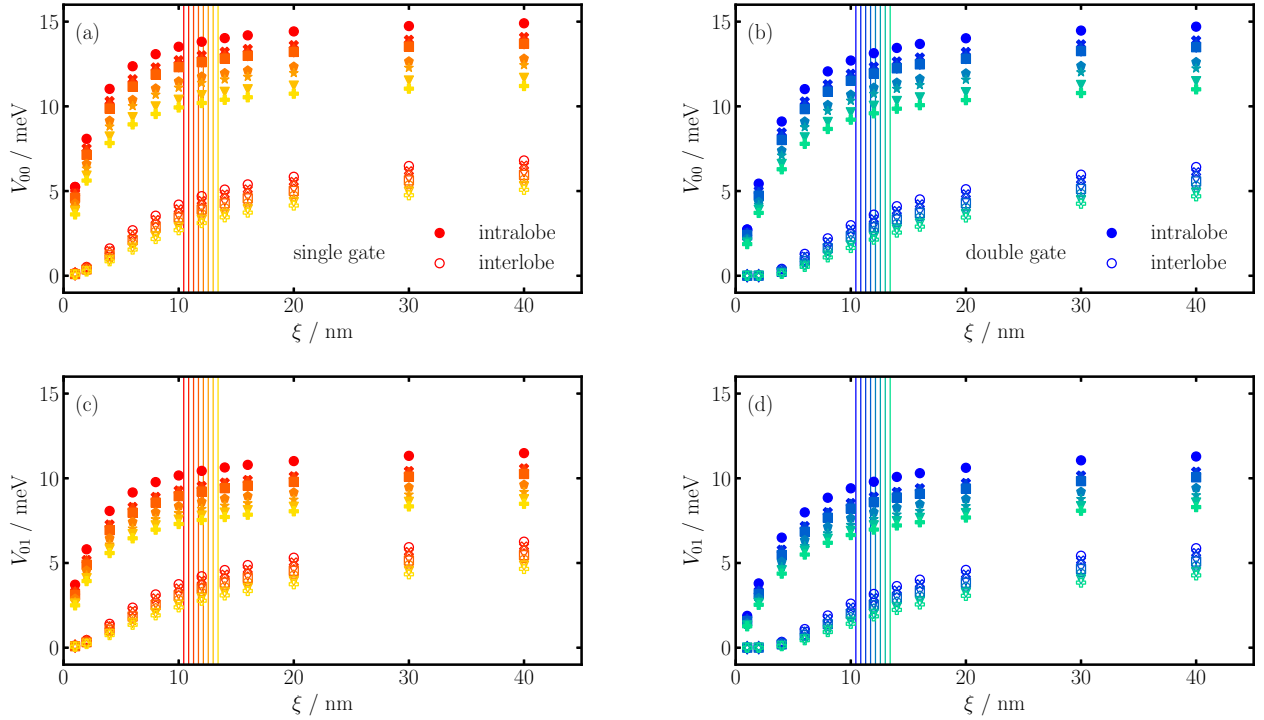


FIG. 6. Intralobe (closed symbols) and interlobe (open symbols) contributions to the on-site Hubbard parameter V_{00} (a),(b) and nearest-neighbor Hubbard parameter V_{01} (c),(d) as a function of gate separation ξ for the studied twist angles (same color and symbol coding for the different twist angles as Fig. 4). The panels in the left-hand (right-hand) column are for the single-gate (double-gate) configuration. The vertical lines correspond to the moiré unit cell length for each twist angle.

The nearest-neighbor Hubbard parameter V_{01} [Figs. 4(c) and 4(d)] and, therefore, also the long-ranged corrected on-site Hubbard parameter $U^* = V_{00} - V_{01}$ [Figs. 4(e) and 4(f)] have a similar dependence on the gate separation as the on-site Hubbard parameter V_{00} . This similarity can be understood from the three-lobe structure of the Wannier functions [28,29,31,34]: the predominant contribution to the Hubbard parameters comes from the overlap of lobes that are centered on the same moiré lattice site (intralobe contributions) plus contributions from the overlap of lobes centered on neighboring moiré lattice sites (interlobe contributions) [31]. In the case of the on-site parameter V_{00} , there are three intralobe and six first-nearest neighbor interlobe interactions, while for

the nearest-neighbor parameter V_{01} , there are two intralobe interactions, six first-nearest-neighbor interlobe interactions and one second nearest-neighbor interlobe interaction.

To make the larger reduction of V_{01} compared to V_{00} more explicit, in Fig. 5 we display the on-site Hubbard parameter in units of the on-site Hubbard parameter in the Coulomb limit, $\tilde{V}_{00} = V_{00}(\xi)/V_{00}(\infty)$, over the next-nearest Hubbard parameter in units of the next-nearest Hubbard parameter in the Coulomb limit, $\tilde{V}_{01} = V_{01}(\xi)/V_{01}(\infty)$; again the subfigures are as a function of distance to the gate and all the studied twist angles are shown, with (a) corresponding to the single gate device and (b) to the double gate device. It is evident from this plot that $\tilde{V}_{00}/\tilde{V}_{01}$ increases as the distance to the gate is

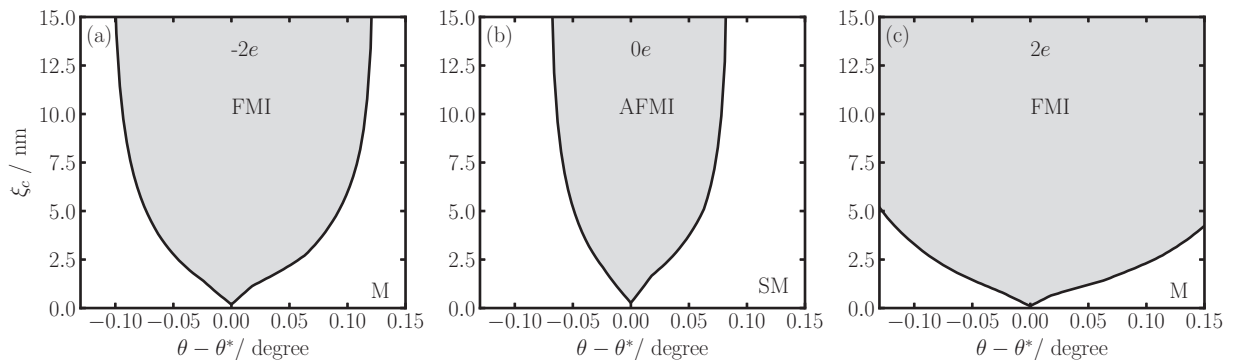


FIG. 7. Critical value of gate separation ξ_c as a function of twist angle from the magic angle for two additional electrons per moiré unit cell ($-2e$, left panel), charge neutrality ($0e$, middle panel), and two additional holes per moiré unit cell ($2e$, right panel), for a device in the double-gate configuration at a temperature of $T \approx 0.3$ K. In the grey regions, FMI denotes a ferromagnetic insulator and AFMI denotes an antiferromagnetic insulator, while in the white regions, M denotes metal and SM denotes semimetal.

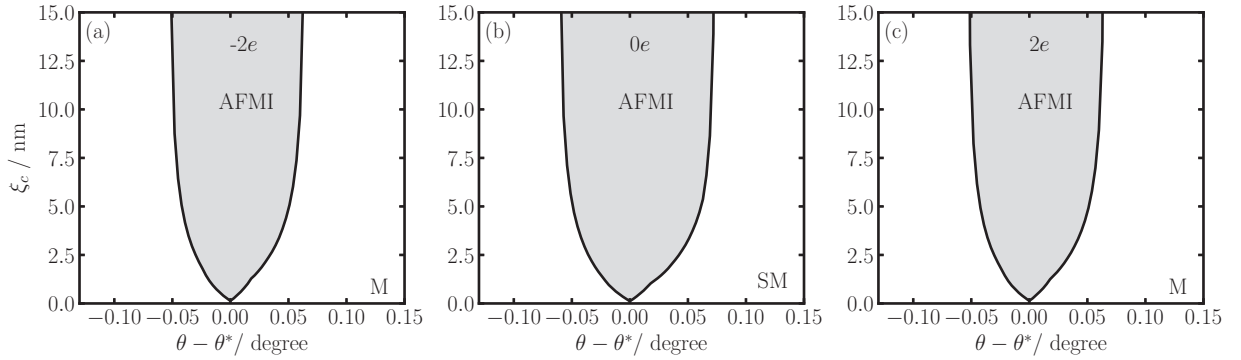


FIG. 8. Critical value of gate separation as a function of twist angle from the magic angle for two additional electrons per moiré unit cell ($-2e$, left panel), charge neutrality ($0e$, middle panel), and two additional holes per moiré unit cell ($2e$, right panel), for a device in the single-gate configuration at a temperature of $T \approx 5$ K. In the grey regions tBLG is an antiferromagnetic insulator (AFMI), while in the white regions, M denotes metal and SM denotes semimetal.

reduced. Therefore, \tilde{V}_{01} (which also means V_{01}) is decreasing more than \tilde{V}_{00} (and therefore V_{00}).

Figure 6 shows the inter- and intralobe contributions to V_{00} and V_{01} for both device configurations [(a),(c) single-gate; (b),(d) double-gate]. These contributions were calculated from the method suggested in Ref. [31], but where the image-charge potential was used in place of the Coulomb potential [28]. As can be seen, the intralobe contributions are larger than the interlobe contributions for all cases [28]. As the distance to the gate is reduced (for separations around the moiré length scale), the interlobe contributions are suppressed more than the intralobe contributions. At separations much smaller than the moiré length scale, the intralobe contributions are significantly truncated.

APPENDIX B: CRITICAL GATE SEPARATION FOR THE DOUBLE-GATE CONFIGURATION

In Fig. 7 we show the critical gate separation for the double gate as a function of twist angle from the magic angle. The plots are qualitatively similar to those of the single-gate configuration (Fig. 3). These plots were made by interpolating $U^*(\xi, \theta)$ linearly in θ and with cubic splines in ξ . We also

fitted $t(\theta) = \Delta(\theta)/6$, where Δ is the bandwidth of the flat bands from our tight-binding model, with a cubic spline as a function of θ . The roots of $U^*(\xi, \theta) - t(\theta)U/t_G$ were found as a function of θ and ξ , where U is the critical value of the interaction from Ref. [27] (which is different for each value of the doping and twist angle, although we only use the values for a twist angle of 1.05° here), and t_G is the hopping parameter of graphene. Note that using the critical values from Ref. [27] is an approximation, since the values stated there are for atomic orbitals, but we are assuming that these values transfer to the moiré flat band orbitals. Additional twist angle dependence of these phase diagrams will also come through using critical values of U (as a function of twist angle) calculated using the methods outlined in Ref. [27]. It is expected that the critical values of U will increase away from the magic angle, and therefore, larger gate separations would be required to reach the critical value.

APPENDIX C: CRITICAL GATE SEPARATION PHASE DIAGRAM AT HIGHER TEMPERATURE

In this section, we discuss the dependence of the phase diagram of tBLG on temperature. Specifically, we use the

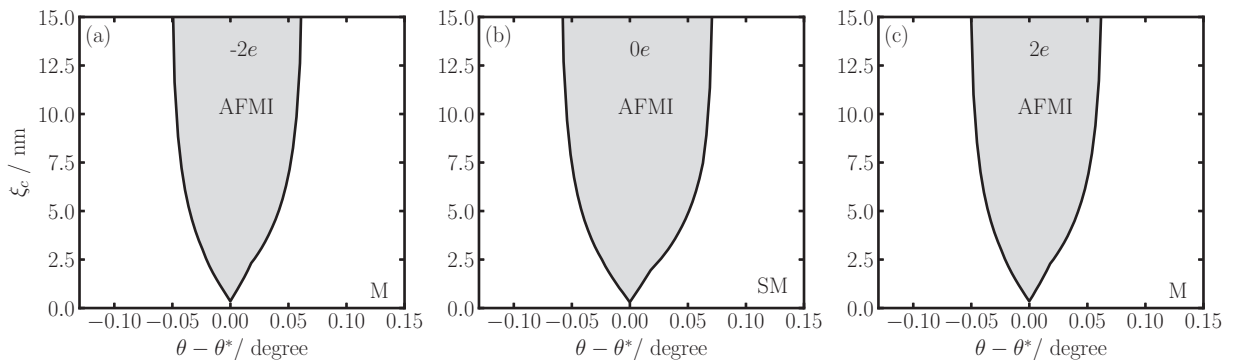


FIG. 9. Critical value of gate separation as a function of twist angle from the magic angle for two additional electrons per moiré unit cell ($-2e$, left panel), charge neutrality ($0e$, middle panel), and two additional holes per moiré unit cell ($2e$, right panel), for a device in the double-gate configuration at a temperature of $T \approx 5$ K. In the grey regions tBLG is an antiferromagnetic insulator (AFMI), while in the white regions, M denotes metal and SM denotes semimetal.

critical value of U at $T = 5$ K [27] which approximately corresponds to the experimentally observed transition temperature of the correlated insulator state. Figures 8 and 9 show the resulting phase diagrams for single and double gate devices, respectively. We find that the results for both device types are

quite similar. In contrast to the low-temperature result (Figs. 3 and 7), the correlated-insulator state at charge neutrality is not screened out by the gate while the insulator states in the doped system disappear. This is in qualitative agreement with recent experimental measurements [42,43].

-
- [1] Y. Cao, V. Fatemi, A. Demir, S. Fang, S. L. Tomarken, J. Y. Luo, J. D. Sanchez-Yamagishi, K. Watanabe, T. Taniguchi, E. Kaxiras, R. C. Ashoori, and P. Jarillo-Herrero, *Nature (London)* **556**, 80 (2018).
- [2] Y. Cao, V. Fatemi, S. Fang, K. Watanabe, T. Taniguchi, E. Kaxiras, and P. Jarillo-Herrero, *Nature (London)* **556**, 43 (2018).
- [3] M. Yankowitz, S. Chen, H. Polshyn, Y. Zhang, K. Watanabe, T. Taniguchi, D. Graf, A. F. Young, and C. R. Dean, *Science* **363**, 1059 (2019).
- [4] X. Lu, P. Stepanov, W. Yang, M. Xie, M. A. Aamir, I. Das, C. Urgell, K. Watanabe, T. Taniguchi, G. Zhang, A. Bachtold, A. H. MacDonald, and D. K. Efetov, *Nature (London)* **574**, 653 (2019).
- [5] Y. Xie, B. Lian, B. Jäck, X. Liu, C.-L. Chiu, K. Watanabe, T. Taniguchi, B. A. Bernevig, and A. Yazdani, *Nature (London)* **572**, 101 (2019).
- [6] A. Kerelsky, L. J. McGilly, D. M. Kennes, L. Xian, M. Yankowitz, S. Chen, K. Watanabe, T. Taniguchi, J. Hone, C. Dean, A. Rubio, and A. N. Pasupathy, *Nature (London)* **572**, 95 (2019).
- [7] Y. Jiang, X. Lai, K. Watanabe, T. Taniguchi, K. Haule, J. Mao, and E. Y. Andrei, *Nature (London)* **573**, 91 (2019).
- [8] S. Carr, S. Fang, P. Jarillo-Herrero, and E. Kaxiras, *Phys. Rev. B* **98**, 085144 (2018).
- [9] Y. D. Liao, Z. Y. Meng, and X. Y. Xu, *Phys. Rev. Lett.* **123**, 157601 (2019).
- [10] X. Y. Xu, K. T. Law, and P. A. Lee, *Phys. Rev. B* **98**, 121406(R) (2018).
- [11] D. M. Kennes, J. Lischner, and C. Karrasch, *Phys. Rev. B* **98**, 241407(R) (2018).
- [12] Y. Sherkunov and J. J. Betouras, *Phys. Rev. B* **98**, 205151 (2018).
- [13] J. Kang and O. Vafek, *Phys. Rev. Lett.* **122**, 246401 (2019).
- [14] J. González and T. Stauber, *Phys. Rev. Lett.* **122**, 026801 (2019).
- [15] C.-C. Liu, L.-D. Zhang, W.-Q. Chen, and F. Yang, *Phys. Rev. Lett.* **121**, 217001 (2018).
- [16] M. Xie and A. H. MacDonald, *Phys. Rev. Lett.* **124**, 097601 (2020).
- [17] B. Padhi, C. Setty, and P. W. Phillips, *Nano Lett.* **18**, 6175 (2018).
- [18] Y. W. Choi and H. J. Choi, *Phys. Rev. B* **98**, 241412(R) (2018).
- [19] H. C. Po, L. Zou, A. Vishwanath, and T. Senthil, *Phys. Rev. X* **8**, 031089 (2018).
- [20] J. M. Pizarro, M. J. Calderón, and E. Bascones, *J. Phys. Commun.* **3**, 035024 (2019).
- [21] F. Wu, A. H. MacDonald, and I. Martin, *Phys. Rev. Lett.* **121**, 257001 (2018).
- [22] M. Ochi, M. Koshino, and K. Kuroki, *Phys. Rev. B* **98**, 081102(R) (2018).
- [23] F. Wu, *Phys. Rev. B* **99**, 195114 (2019).
- [24] B. Roy and V. Juričić, *Phys. Rev. B* **99**, 121407(R) (2019).
- [25] F. Guinea and N. R. Walet, *Proc. Natl. Acad. Sci. USA* **115**, 13174 (2018).
- [26] J. M. Pizarro, M. Rösner, R. Thomale, R. Valentí, and T. O. Wehling, *Phys. Rev. B* **100**, 161102(R) (2019).
- [27] L. Klebl and C. Honerkamp, *Phys. Rev. B* **100**, 155145 (2019).
- [28] Z. A. H. Goodwin, F. Corsetti, A. A. Mostofi, and J. Lischner, *Phys. Rev. B* **100**, 121106(R) (2019).
- [29] Z. A. H. Goodwin, F. Corsetti, A. A. Mostofi, and J. Lischner, *Phys. Rev. B* **100**, 235424 (2019).
- [30] G. Trambly de Laissardière, D. Mayou, and L. Magaud, *Phys. Rev. B* **86**, 125413 (2012).
- [31] M. Koshino, N. F. Q. Yuan, T. Koretsune, M. Ochi, K. Kuroki, and L. Fu, *Phys. Rev. X* **8**, 031087 (2018).
- [32] N. Marzari, A. A. Mostofi, J. R. Yates, I. Souza, and D. Vanderbilt, *Rev. Mod. Phys.* **84**, 1419 (2012).
- [33] G. Pizzi *et al.*, *J. Phys.: Condens. Matter* **32**, 165902 (2020).
- [34] J. Kang and O. Vafek, *Phys. Rev. X* **8**, 031088 (2018).
- [35] J. Xue, J. Sanchez-Yamagishi, D. Bulmash, P. Jacquod, A. Deshpande, K. Watanabe, T. Taniguchi, P. Jarillo-Herrero, and B. J. LeRoy, *Nat. Mater.* **10**, 282 (2011).
- [36] R. E. Throckmorton and O. Vafek, *Phys. Rev. B* **86**, 115447 (2012).
- [37] J. Hubbard, *Proc. R. Soc. London, Ser. A* **276**, 238 (1963).
- [38] J. Hubbard, *Proc. R. Soc. London, Ser. A* **277**, 237 (1964).
- [39] M. Schüler, M. Rösner, T. O. Wehling, A. I. Lichtenstein, and M. I. Katsnelson, *Phys. Rev. Lett.* **111**, 036601 (2013).
- [40] T. C. Lang, Z. Y. Meng, M. M. Scherer, S. Uebelacker, F. F. Assaad, A. Muramatsu, C. Honerkamp, and S. Wessel, *Phys. Rev. Lett.* **109**, 126402 (2012).
- [41] N. F. Q. Yuan and L. Fu, *Phys. Rev. B* **98**, 045103 (2018).
- [42] P. Stepanov, I. Das, X. Lu, A. Fahimniya, K. Watanabe, T. Taniguchi, F. H. L. Koppens, J. Lischner, L. Levitov, and D. K. Efetov, *arXiv:1911.09198*.
- [43] Y. Saito, J. Ge, K. Watanabe, T. Taniguchi, and A. F. Young, *arXiv:1911.13302*.
- [44] P. B. Allen and R. C. Dynes, *Phys. Rev. B* **12**, 905 (1975).